Electronic
Research Archive

https://www.aimspress.com/journal/era

ERA, 33(10): 6476–6492.
DOI: 10.3934/era.2025285
Received: 09 August 2025
Revised: 07 October 2025
Accepted: 21 October 2025
Published: 29 October 2025

Research article

Encoding scheme-dependent effects of input pattern pairs on pattern separation in the dentate gyrus neuronal network

Huimin Bai[1] **and Kai Yang**[2,*]

[1] Department of Cybersecurity Defense, Shanxi Police College, Taiyuan 030401, China
[2] School of Science, Beijing University of Posts and Telecommunications, Beijing 100876, China

* **Correspondence:** Email: kai_yang@bupt.edu.cn.

Abstract: The ability to discriminate highly similar memories depends critically on pattern separation mediated by the dentate gyrus (DG). Although intrinsic neural mechanisms have been extensively studied, the influence of external input patterns on this process is often overlooked. Here, we established a biologically plausible DG model, subjected it to input pattern pairs with varying degrees of overlap, and examined the firing properties of granule cells (GCs) as output patterns. Based on the analysis of population coding, we observed that as the overlap between input pairs decreased, both the separation distance and orthogonalization level increased, indicating enhanced separation performance. Subsequently, from the perspective of rate coding, we computed the mean firing rate of individual GC to paired inputs and statistically analyzed the distributions of mean firing rates and their pairwise differences across GCs. Our results showed that these firing rate metrics unaffected by variations in input overlap. However, the Pearson correlation coefficient and mutual information between GC ensembles were significantly influenced, with both measures decreasing as input overlap is reduced. We also found that high-overlap inputs ($> 70\%$) induced substantial firing rate variability in individual GC, which predominantly manifested as rate remapping. Furthermore, clustering analysis based on time-windowed firing rates demonstrated that pattern separation does not alter the structural characteristics of GCs, with similar cluster configurations emerging across different input overlap conditions. Together, these findings provided a detailed characterization of GC firing properties during pattern separation.

Keywords: pattern separation; input pattern pairs; population coding; rate coding; neuronal network

1. Introduction

The hippocampal, anatomically defined by the dentate gyrus (DG) and cornu ammonis subfields (CA1-CA4), serves as a central hub for the encoding, consolidation, and retrieval of spatial and episodic memories [1, 2]. Within this structure, the CA3 region is widely regarded as an auto-associative memory network. This characterization stems from the dense recurrent collateral connections formed among its pyramidal neurons [3, 4]. This specific neural architecture facilitates two primary operational modes: memory encoding and memory retrieval. During encoding, afferent information induces synaptic plasticity at the recurrent collaterals, thereby storing memory traces. Conversely, during retrieval, an incomplete input cue can activate a subset of neurons. This partial activation propagates through previously potentiated synaptic pathways, enabling the recapitulation of the complete stored memory pattern, a process termed pattern completion [5–7]. Critically, effective memory retrieval depends on mnemonic cues selectively engaging specific neuronal ensembles. These ensembles subsequently recruit associated neurons via the pre-wired recurrent circuitry to reconstruct the entire memory representation. The fidelity of this retrieval process relies fundamentally on the distinctiveness of the neural ensembles representing individual memories. If highly overlapping ensembles encode similar memories, interference can occur during recall, impairing retrieval accuracy [8]. To counteract this potential interference, it is proposed that the similarity of incoming information must be reduced prior to storage. This transformation of analogous inputs into more distinct neural representations is known as pattern separation [2, 9–11].

The DG contributes critically to pattern separation, with granule cells (GCs) serving as the main neuronal subtype that carries sensory signals from the entorhinal cortex (EC) to CA3 region via powerful mossy fiber [12]. Beyond GCs, the DG incorporates mossy cells (MCs) and diverse inhibitory interneuron subtypes [13]. A defining functional characteristic of the DG is sparse coding, observed experimentally as the activation of only a minor fraction (5%) of GCs during specific behavioral epochs [14, 15]. This remarkably low population activity density is computationally advantageous: it permits highly differentiated sensory inputs to be mapped onto largely nonoverlapping ensembles of GCs. Consequently, sparse coding is a fundamental mechanism enabling effective pattern separation within the DG [16, 17].

Computational models of pattern separation function in the DG have garnered increasing attention, with the earliest foundational work dating back to Marr's seminal 1971 model of paleocortical memory mechanisms, which introduced a mathematical framework based on binary neurons and synapses and first explored the DG's role in memory processing [18]. Since then, such models have evolved substantially from abstract representations to biologically complex neuronal networks [19–21]. A key advancement was achieved by Myers and Scharfman, who constructed the first large-scale neural network incorporating hilar cells to simulate DG-mediated pattern separation [22]. Later extensions of this model explored how feedback projections originating in the CA3 region influence DG pattern separation [23]. Research demonstrates that these CA3-to-DG feedback pathways enhance pattern separation efficacy by boosting local inhibition. Furthermore, the impact of hilar ectopic granule cells (hEGCs) on pattern separation was also investigated [24]. Research revealed that even a very small number of hEGCs is sufficient to cause pattern separation failure. Hummos et al. constructed an EC-DG-CA3 neuronal network model based on the Izhikevich neuron model [25]. By incorporating inhibitory microcircuit mechanisms more closely aligned with biological reality, this model demonstrated that high levels of acetylcholine (ACh) can enhance pattern separation efficiency. More precise modeling of neurons is also a current trend, which facilitates the investigation of how intrinsic neuronal properties and morphological characteristics contribute to pattern separation. Chavlis et al. modeled GC as a leaky integrate-and-fire (LIF) somatic compartment coupled with a variable number of dendritic compartments, and the results show that the presence of dendrites is beneficial for pattern separation [15].

So far, based on the aforementioned studies, we have come to realize that there are numerous factors that affect pattern separation function, including dendritic structure, specific types of neurons, and so on. However, we also note that current investigations predominantly focus on the intrinsic mechanisms within the DG. In contrast, research investigating how pairs of input patterns from the EC, which constitutes the principal afferent source to the DG, influence both GC firing dynamics and pattern separation efficacy remains insufficient. Furthermore, existing studies largely operate within the framework of population coding, with discussions concerning rate coding also being notably limited. A critical methodological consideration is that divergent neural coding frameworks inherently demand customized quantification approaches to evaluate pattern separation. Addressing these currently inadequately characterized methodological requirements defines the central focus of this investigation.

2. Model

2.1. The DG neural network model

The computational framework for our DG model implements core design principles established in seminal work by Myers and Scharfman [22, 23]. This architecture incorporates distinct neuronal populations: granular layer principal neurons (GCs) alongside basket cells (BCs), complemented by polymorphic layer excitatory MCs and hilar perforant path-associated cells (HIPP cells). To ensure neurobiological fidelity, population sizes for each neuronal class and their inter-neuronal connection probabilities were constrained to match empirical anatomical and physiological observations [15].

The computational model comprises a total of 2000 GCs, corresponding to a scaling factor of 1:500 relative to the estimated GC population in the rodent DG. This constrained population size was chosen to balance biological plausibility in simulating pattern separation with computational feasibility. Reflecting the septotemporal organization of the DG, GCs are distributed across 100 discrete functional modules along the longitudinal axis, each consisting of 20 neuronal units [15]. This modular architecture mimics the intrinsic columnar organization of the DG and supports its spatial coding functions. Each module also contains one BC, resulting in a total of 100 BCs throughout the network. Within each module, a competitive "winner-take-all" mechanism is implemented: individual BCs integrate excitatory inputs from all 20 GCs and provide feedback inhibition to them [26]. This localized inhibitory circuit plays a critical role in regulating GC activity to enforce sparse coding and improve pattern separation efficiency. Based on anatomical data from the rat DG, which contains approximately 30,000–50,000 MCs and 12,000 HIPP cells, our model incorporates 80 MCs and 40 HIPP cells [27, 28]. Synaptic connectivity follows experimentally informed rules: GCs project to MCs with a probability of 20%; each MC establishes all-to-all connections with all BCs; and HIPP cells form feedback connections to GCs with a synaptic probability of 20% [4, 17].

2.2. Construction of input pattern pairs

The DG receives its predominant cortical input from Layer II of the EC. In modeling this pathway, the biological 200,000 neurons in rat EC Layer II were reduced to 400 model units. Given experimental reports of 10% spontaneous activation rates, 40 randomly chosen units generated Poisson-process spike trains (mean rate: 40 Hz) [29–31]. GCs received excitatory projections from stochastically sampled 20% of EC units (80 cells), while HIPP cells were similarly innervated at $1/5$ probability. The final configuration of the DG neuronal network model incorporating EC inputs is illustrated in Figure 1.

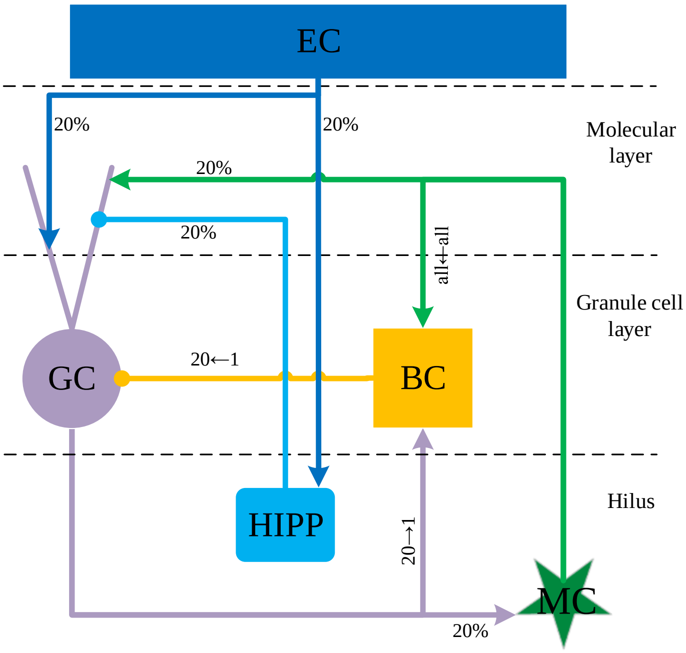

Figure 1. The schematic diagram of the connectivity architecture within the DG neural network. The DG network receives similar input pattern pairs from the EC, and arrows and circles denote excitatory and inhibitory synaptic connections. It should be emphasized that the diagram is a conceptual representation and does not depict the dendritic structures of GCs.

Within our computational framework, input patterns are represented by activated neurons in the Layer II of the EC, while output patterns are formed by GCs in the DG. Effective pattern separation is achieved when the DG generates output representations with reduced overlap and increased distinctness compared to two highly correlated input patterns. Each experimental trial consists of paired simulations in which two related yet distinct input configurations are delivered to the network, evoking corresponding spiking responses in GC populations. The similarity between input patterns is systematically regulated by parameter P, which quantifies their probabilistic overlap. Specifically, input pattern A is generated through random selection of 40 active neurons from the EC Layer II population. We engineered input pattern B to overlap input pattern A at five defined levels: 80% (32 shared neurons), 70% (28), 60% (24), 50% (20), and 40% (16). Spatial configurations of these patterns are visualized in Figure 2.

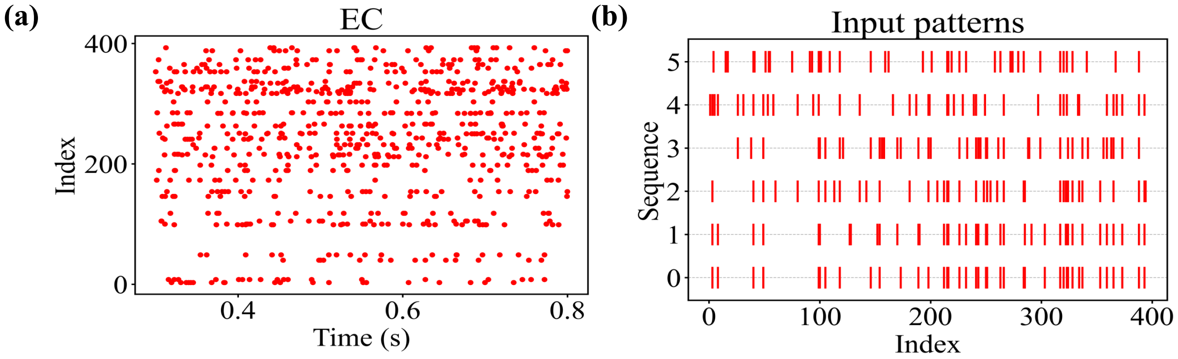

Figure 2. Constructed input pattern pairs. (a) The raster plot of 40 randomly selected neurons in input pattern A, and each active neuron fires as a Poisson process with a mean rate of 40 Hz. (b) Input patterns A and B exhibit different degrees of overlap, and the overlap degree ranges from 80% to 40%.

2.3. The neuron model

To ensure neurobiological fidelity, model parameters were experimentally bounded to recapitulate observed neuronal discharge dynamics. Balancing complexity and fidelity, we implemented the adaptive exponential integrate-and-fire (AdEx) model [32]. This framework captures heterogeneous electrophysiological profiles with computational efficiency, enabling multi-scale mechanistic analysis. Crucially, pattern separation quantification prioritizes GCs' binary firing states over precise timing. Validation thus focuses on mean firing rate concordance with empirical data. Neuronal dynamics are governed by:

$$\begin{cases} C_m\dfrac{dV_m}{dt} = g_l(E_l - V_m) + g_l\Delta_T exp(\dfrac{V_m - V_T}{\Delta_T}) \\ \qquad\qquad + \sum I_{syn} - \omega \\ \tau_\omega\dfrac{d\omega}{dt} = \alpha(V_m - E_l) - \omega. \end{cases} \tag{2.1}$$

Table 1. Numerical values of model parameters.

Parameters	GC	MC	BC	HIPP
$C_m(nF)$ membrane capacitance	0.00678	0.2521	0.1793	0.0584
$g_l(nS)$ leak conductance	0.2639	4.53	18.054	1.93
$E_l(mV)$ membrane potential	-87	-64	-52	-59
$\Delta_T(mV)$ spike slope factor	–	2	2	2
$V_T(mV)$ effective threshold	-56	-42	-39	-50
$\tau_\omega(mS)$ adaptation time constant	45	180	100	93
$\alpha(nS)$ adaptation coupling coefficient	2	2	0.1	0.82
$b(nA)$ spike-triggered adaptation strength	0.045	0.0829	0.0205	0.015
$V_{reset}(mV)$ reset potential	-74	-49	-45	-56

Neuronal firing occurs upon membrane potential (V_m) attaining threshold V_T. Post-spike, two processes ensue: 1) V_m reverts to reset potential V_{reset}, 2) adaptation current ω increases by increment b, where b represents spike-evoked adaptation intensity. Complete parameter values are documented in Table 1.

2.4. The synapse model

Neurochemical signaling between neurons occurs predominantly through synaptic transmission, where intercellular signaling dynamics are governed by ligand-receptor binding kinetics. In our DG network model-incorporating both glutamatergic and GABAergic populations-the aggregate postsynaptic current ($\sum I_{syn}$) constitutes the linear superposition of three physiologically distinct conductance pathways:

$$\sum I_{syn} = I_{AMPA} + I_{NMDA} + I_{GABA} \tag{2.2}$$

where I_{AMPA} and I_{NMDA} denote glutamate-mediated excitatory currents, and I_{GABA} embodies GABAergic inhibitory signaling. Given the predominance of GABA$_A$ receptors in dentate inhibition, our computational representation exclusively incorporates this receptor subtype [15]. As ionotropic channels, their postsynaptic currents instantiate the governing equations:

$$I_{syn} = -g_{syn}(t)[V(t) - E_{syn}] \tag{2.3}$$

where the synaptic conductance g_{syn} parameterizes the channel permeability and E_{syn} denotes the ionic reversal potential.

For AMPA and GABA$_A$ receptors, conductance dynamics are governed by [33]:

$$\begin{aligned} g_{AMPA/GABA}(t) =& g_{max(AMPA/GABA)} \\ & * (\exp(-\frac{t}{\tau_{decay}}) - \exp(-\frac{t}{\tau_{rise}})) \end{aligned} \tag{2.4}$$

and this dual-exponential formulation captures distinct rising (τ_{rise}) and decay (τ_{decay}) phases. NMDA receptors exhibit additional voltage-dependent magnesium blockade:

$$\begin{aligned} g_{NMDA}(t) =& g_{max(NMDA)} \\ & * (\exp(-\frac{t}{\tau_{decay}}) - \exp(-\frac{t}{\tau_{rise}})) \\ & * (\frac{1}{1 + \eta[Mg^{2+}]_o exp(-\gamma V)}) \end{aligned} \tag{2.5}$$

where η modulates magnesium sensitivity, γ controls voltage-dependence steepness, and $[Mg^{2+}]_o$ is extracellular magnesium concentration.

Parameter values were derived from established electrophysiological evidence [15, 34–37]. For BCs, MCs and HIPP cells, the magnesium block coefficient η was set to 0.28 mM^{-1}, with voltage sensitivity $\gamma = 0.072\,\text{mV}^{-1}$ and extracellular magnesium concentration $[\text{Mg}^{2+}]_o = 1$ mM. GCs necessitated differential parameterization: $\eta = 0.2\,\text{mM}^{-1}$, $\gamma = 0.04\,\text{mV}^{-1}$, $[\text{Mg}^{2+}]_o = 2$ mM. To address axonal component exclusion in our somatocentric models, interneuronal transmission delays were systematically incorporated.

3. Results

In the following sections, we first analyze GC firing dynamics and pattern separation performance under input patterns of varying overlap, based on population coding principles. To systematically evaluate pattern separation, two quantitative metrics were introduced. We then shift focus to rate coding, offering a detailed characterization of GC firing rate properties along with appropriate quantitative descriptors. Finally, we perform clustering analysis on GC populations using time-windowed firing rates to identify functionally distinct neuronal groups.

3.1. Effect of input pairs overlap on pattern separation in population coding

We applied input pattern pairs with varying degrees of overlap (ranging from 80% to 40%) to the DG neural network. This elicited corresponding firing patterns in the GC population, constituting our output pattern pairs. Subsequently, we quantified both the input and output pattern pairs to derive the pattern separation efficiency. It is widely accepted that pattern separation is achieved through two primary mechanisms mediated by GCs: sparsity and orthogonalization [22]. Accordingly, we employed two distinct quantitative metrics: population distance (D) and cosine similarity (C). These metrics assess different dimensions of pattern separation. When both indicators demonstrate enhanced pattern separation, we can conclusively determine an improvement in pattern separation performance.

Population distance can be expressed in the following form [15]:

$$D_{i/o} = \frac{HD_{i/o}}{2N_{i,o}(1 - s_{i/o})} \tag{3.1}$$

using subscript notation, i denotes input patterns and o represents output patterns. The Hamming distance between corresponding patterns is expressed as $HD_{i/o}$. The denominator includes a factor of 2 to ensure normalization of distance metric D to the range $[0, 1]$. Here, N indicates total neuron count, while sparsity s is defined as the proportion of inactive neurons. GCs are classified as active when generating ≥ 1 spike during stimulus presentation. Pattern separation in the DG neural network is demonstrated when the population distance of output patterns (D_o) surpasses that of input patterns (D_i). The other metric, cosine similarity, is a measure used to assess the directional similarity between two vectors. It quantifies the angular relationship between them by computing the cosine of the angle formed by the vectors. The formula is as follows:

$$\begin{aligned} C_{i/o} &= Cosine\,Similarity(A, B) \\ &= \cos(\theta) \\ &= \frac{A \cdot B}{||A||\,||B||} \end{aligned} \tag{3.2}$$

the numerator signifies the dot product between vectors A and B, reflecting their element-wise alignment, whereas the denominator normalizes this value by the product of their Euclidean magnitudes, ensuring that the similarity metric is invariant to vector scaling. Cosine similarity C takes values in the interval $[-1, 1]$. A value of 1 indicates identical directions, -1 indicates opposite directions, and 0 indicates orthogonality between the vectors. It should be noted that prior to quantification, neuronal states require binary encoding: 400 EC neurons and 2000 GCs are represented with active units as 1 and quiescent units as 0.

Output patterns corresponding to input pairs with varying overlap degrees are visualized in Figure 3. All reported results represent averages over 10 independent simulation trials. In each trial, an 800 ms network simulation was performed with a temporal resolution of 0.1 ms. To ensure dynamical stability, the initial 300 ms of data was excluded from analysis. Spiking activity of GCs during the subsequent 500 ms stimulation window (300–800 ms), evoked by entorhinal cortical inputs, constituted the dataset for further analysis. As shown in Figure 4, the population distance D_o gradually increased, while cosine similarity C_o progressively decreased as input overlap diminished, indicating more distinct separation of output patterns. Furthermore, we consistently observed $D_o > D_i$ and $C_o < C_i$, confirming the effectiveness of the model in performing pattern separation. To further quantify separation performance, we evaluated pattern separation efficiency, defined as the difference between output and input measures either $D_o - D_i$ or $C_o - C_i$. As illustrated in Figure 5, separation efficiency declines as the overlap degree P decreases, reflecting the network's reduced capacity for enhancing separation when input patterns are already highly distinct.

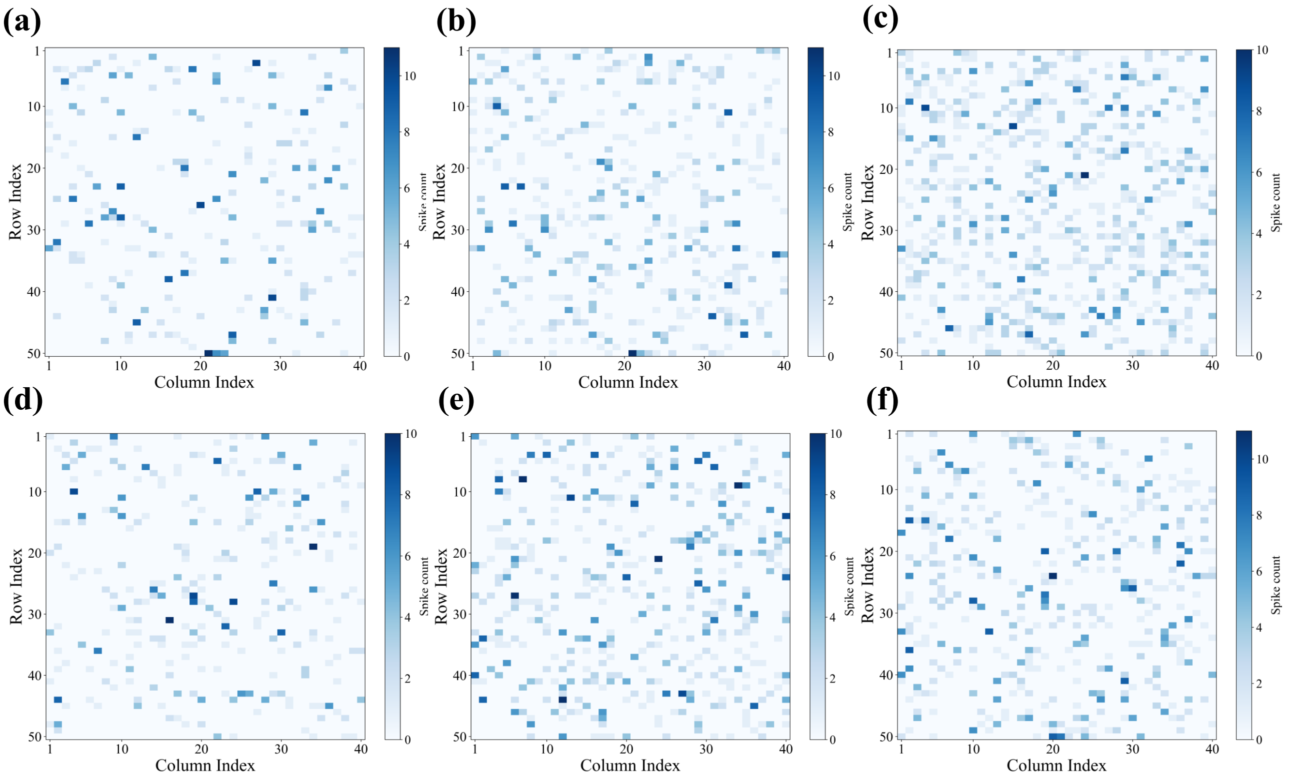

Figure 3. Visualization of output patterns (GCs) evoked by input pairs with varying overlap ratios. (a) Output pattern elicited by input pattern A. (b–f) Output patterns generated by input pattern B, which shared with pattern A predefined proportions of active neurons: 80%, 70%, 60%, 50%, and 40%, respectively.

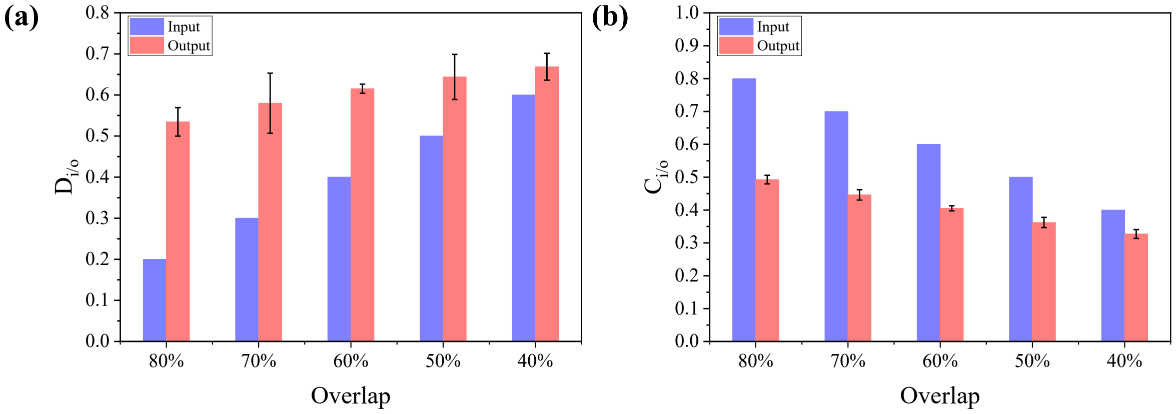

Figure 4. The output patterns' population distance and cosine similarity were evaluated across different overlap percentages *P*.

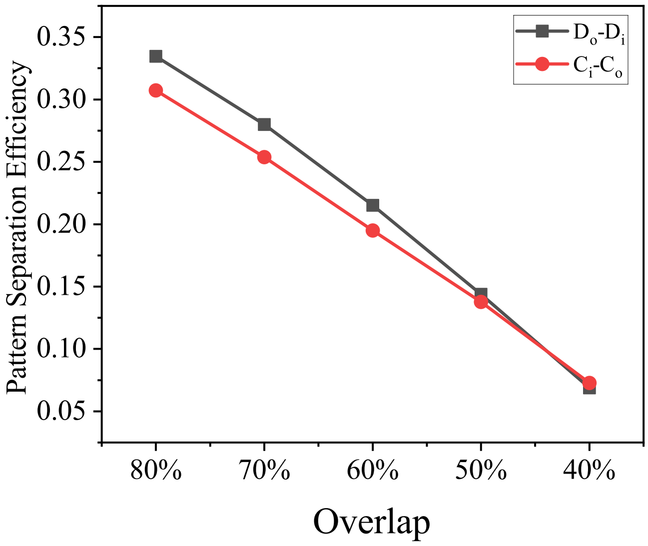

Figure 5. The output patterns' pattern separation efficiency were evaluated across different overlap percentages *P*.

3.2. *Effect of input pairs on the firing rates of GC*

All analyses were conducted using population coding principles, with neuronal activation defined by the occurrence of one or more spikes. However, given the naturally varying spike counts across active neurons in biological systems, we implemented a more refined rate coding scheme to enable finer discrimination between output patterns. Figure 6(a),(b) displays the average firing rates and their distribution histograms for corresponding GC populations when input patterns A and B share 80% overlap. We computed the difference in average firing rates for each GC between the two input conditions, identifying 1027 neurons with unchanged firing rates and characterizing the resulting difference distribution. The similarity between the two firing rate distributions was quantified using

Jensen–Shannon divergence, yielding a value of 0.0042. Additionally, Pearson correlation analysis of the average firing rates across all 2000 GCs revealed a correlation coefficient of 0.6352. The Jensen–Shannon divergence provides a symmetric measure of distributional similarity, defined as the weighted sum of Kullback-Leibler divergences between each distribution and their average. The mathematical formulation is expressed as follows:

$$JS(P \parallel Q) = \frac{1}{2} D_{KL}(P \parallel M) + \frac{1}{2} D_{KL}(Q \parallel M) \tag{3.3}$$

where $M = (P + Q)/2$. The Jensen-Shannon divergence ranges from 0 to 1, with smaller values indicating greater similarity between the two distributions. The formula for calculating the Pearson correlation coefficient is as follows:

$$r_{xy} = \frac{\sum_{i=1}^{n}(x_i - \bar{x})(y_i - \bar{y})}{\sqrt{\sum_{i=1}^{n}(x_i - \bar{x})^2}\sqrt{\sum_{i=1}^{n}(y_i - \bar{y})^2}}. \tag{3.4}$$

It measures the linear correlation between two variables. Its value ranges from -1 to 1, representing perfect negative correlation, no correlation, and perfect positive correlation, respectively. In this context, it can be used to quantify the similarity between neuronal response patterns under two different input conditions. If a neuron consistently fires at a high or low rate across both conditions while maintaining its relative rank within the population, the correlation will be significantly positive. This indicates that the change in stimulation does not substantially alter the neuron's relative coding role.

At 70% overlap between input patterns A and B, the corresponding GC firing characteristics for pattern B (Figure 6(c)) included 954 neurons with unchanged mean firing rates, a Jensen–Shannon divergence of 0.0080, and a Pearson correlation coefficient of 0.5559. When overlap decreased to 60% (Figure 6(d)), the number of rate-invariant neurons was 1040, with a Jensen–Shannon divergence of 0.0035 and a Pearson correlation of 0.4411. At 50% overlap (Figure 6(e)), 1013 neurons exhibited unchanged firing rates, accompanied by a JensenCShannon divergence of 0.0084 and a Pearson correlation of 0.2699. Finally, under 40% overlap (Figure 6(f)), 996 neurons maintained consistent firing rates, while the Jensen–Shannon divergence measured 0.0032 and the Pearson correlation coefficient was 0.2961.

Based on the aforementioned results, we conclude that as the overlap between input patterns A and B decreases, both the mean firing rates of GCs and the corresponding firing rate distribution histograms remain highly consistent across output patterns. Specifically, neither the number of GCs exhibiting unchanged mean firing rates nor the histogram of firing rate differences shows significant variation. However, a pronounced decrease is observed in the Pearson correlation coefficient between mean firing rates. This suggests that reduced input overlap alters the relative coding roles of neurons, inducing shifts in their firing levels and decreasing the similarity of population-wide response patterns. Therefore, from a rate coding perspective, the Pearson correlation coefficient of GC mean firing rates serves as a suitable quantitative metric for evaluating pattern separation performance, as shown in Figure 7(a). It should be noted that a lower Pearson correlation indicates better pattern separation. We further observed that under high overlap conditions ($> 70\%$), the same GC exhibits considerable variability in average firing rate, with a mean difference exceeding 0.1 Hz. In contrast, this difference is markedly smaller at lower overlap levels. These findings suggest that GCs are more prone to rate remapping when input patterns are highly similar.

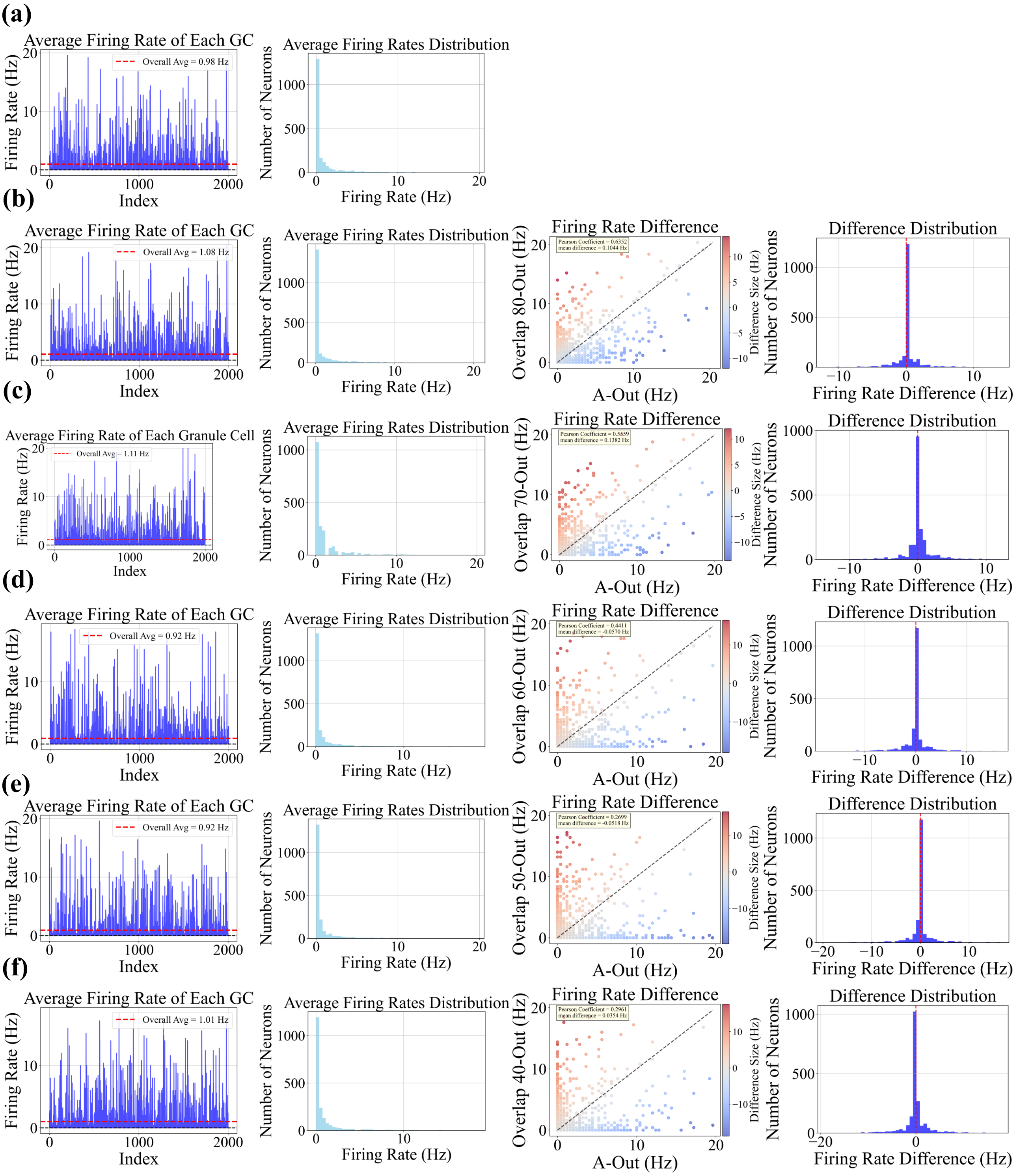

Figure 6. Statistical characterization of GC firing rates across different input patterns. From top to bottom: input pattern *A*, followed by input pattern *B* with overlap degrees decreasing from 80% to 40% relative to *A*. (a) Panels from left to right: mean firing rate and firing rate distribution histogram. (b–f) Additional comparative analyses with input pattern *A*: correlation scatterplot and difference distribution of firing rates.

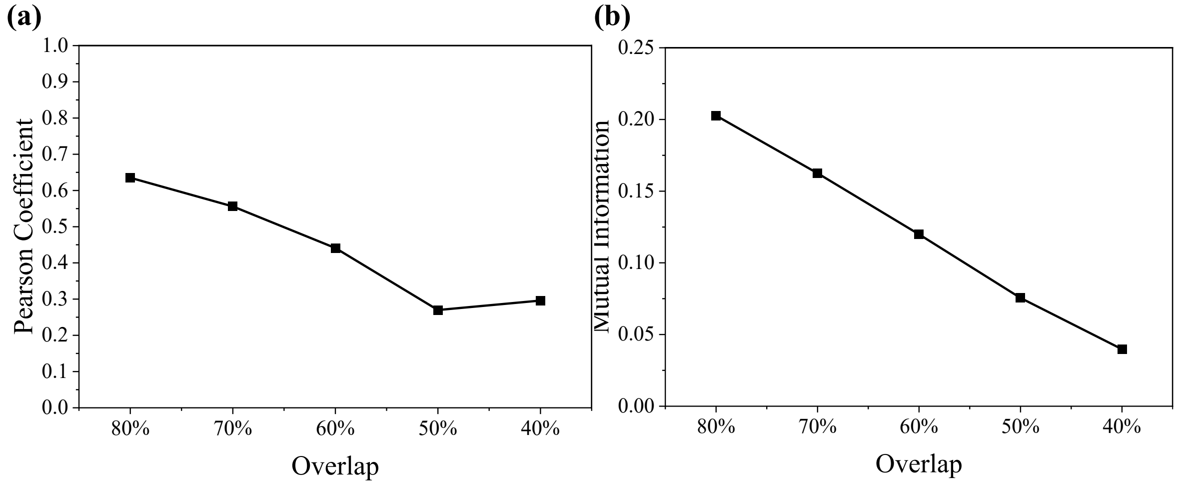

Figure 7. Pearson correlation coefficient and MI at different overlap degree P.

Pearson correlation coefficient measures the linear correlation between two variables. However, neuronal response relationships may exhibit nonlinear characteristics. Therefore, we also employed mutual information (MI) as an additional metric to capture potential relationships that might be missed by Pearson correlation. The mathematical definition of MI is as follows:

$$H(X,Y) = H(X) + H(Y) - I(X;Y). \tag{3.5}$$

We employed the K-Nearest Neighbors (KNN) method for MI estimation. The larger the value of MI, the stronger the dependency between two variables, indicating a greater amount of shared information. Consequently, MI can also be utilized as a metric to quantify pattern separation performance. As shown in Figure 7(b), with the decrease in overlap degree between input pairs, the MI between output pattern pairs decreases, thereby indicating an improvement in pattern separation performance.

3.3. Clustering analysis of GCs based on time-windowed firing rates

To move beyond static mean firing rates, we analyzed time-resolved firing dynamics of GCs using sliding fixed-width time windows, capturing temporal activity patterns that provide richer information than stationary averages. Cluster analysis was subsequently performed on these temporal firing patterns to identify distinct activity modes and potential functional groupings. Methodologically, we first applied principal component analysis (PCA) for dimensionality reduction after data standardization, retaining 95% of the variance to eliminate redundancy and noise. The optimal number of clusters was determined by evaluating silhouette scores across 2–5 candidate clusters, where the silhouette coefficient quantifies clustering quality by measuring the balance between intra-cluster cohesion and inter-cluster separation (values approaching 1 indicate superior separation) [38]. K-means clustering was then employed to partition neurons into distinct functional populations. Finally, we quantified both neuronal counts and characteristic average firing patterns for each identified cluster.

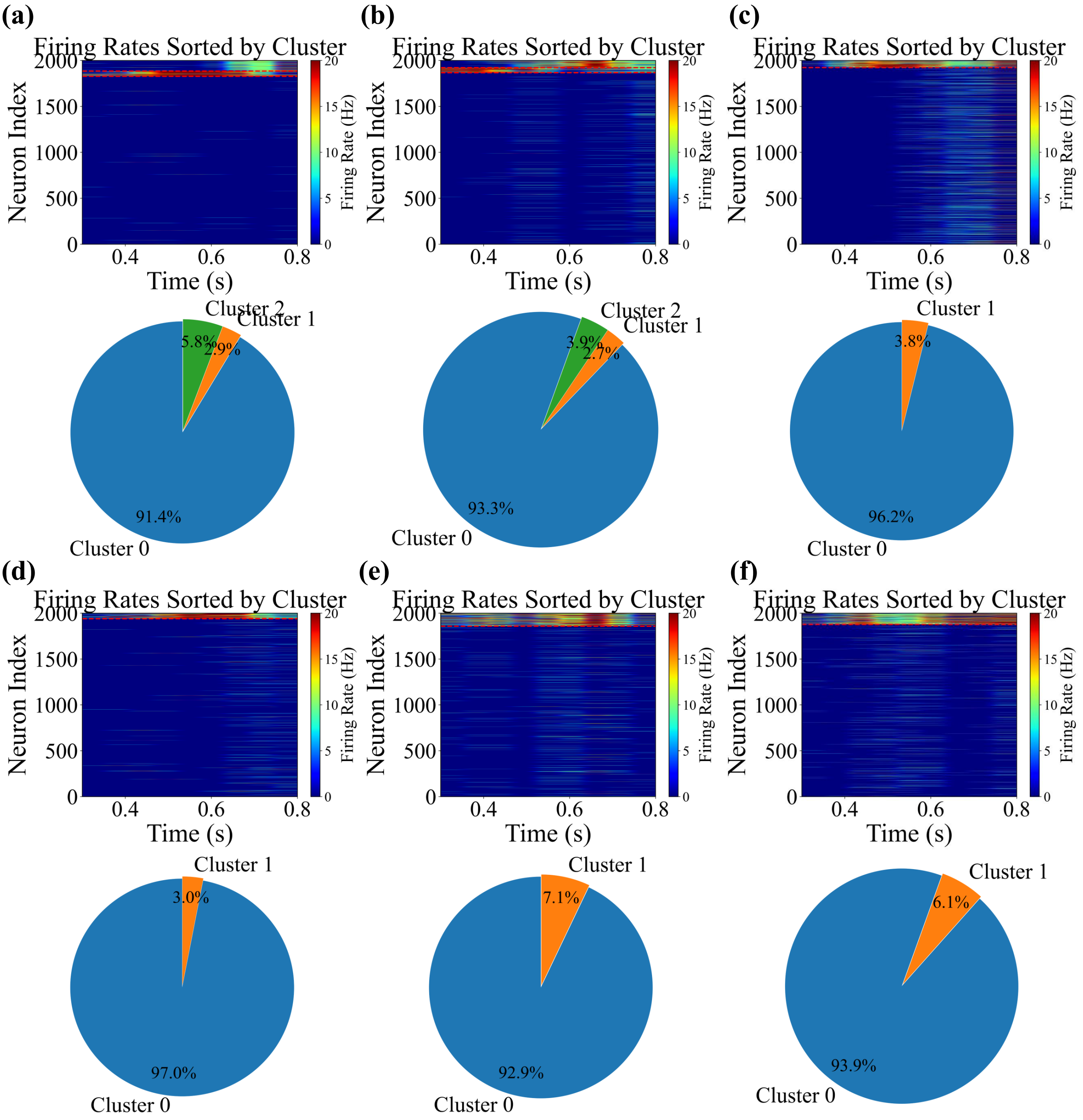

Figure 8. Time-windowed firing rates of GCs and corresponding clustering results under different input patterns. (a) Input pattern A. (b–f) Input pattern B with progressively decreasing overlap percentages relative to pattern A: 80%, 70%, 60%, 50%, and 40%, respectively.

The time-windowed firing rates of GCs and the corresponding clustering analysis results under different input patterns are shown in Figure 8. Clustering analyses of 2000 GCs reveal distinct groups across input patterns. For input pattern A (silhouette coefficient = 0.9145), three clusters emerge: 0 (1,828; 91.4%) with low-intensity firing (0.04 Hz), 1 (57; 2.9%) exhibiting mid-task activation and high-intensity firing (13.43 Hz), and 2 (115; 5.8%) with late-task activation and moderate-intensity firing (3.40 Hz); for input pattern *B* with 80% overlap (silhouette = 0.8550), clusters are: 0 (1,867; 93.3%) low-intensity (0.27 Hz), 1 (55; 2.8%) early-task activation and high-intensity (10.67 Hz), and 2 (78; 3.9%) late-task activation and high-intensity (7.93 Hz); for input pattern *B* with 70% overlap (silhouette = 0.8233), two clusters are identified: 1 (1,924; 96.2%) low-intensity (0.91 Hz) and 2 (76; 3.8%) mid-task activation and high-intensity (10.76 Hz); for input pattern *B* with 60% overlap (silhouette = 0.8233), clusters are: 0 (1,940 cells; 97.0%) low-intensity firing (mean rate: 0.27 Hz) and cluster 1 (60; 3.0%) mid-task activation with high-intensity firing (11.56 Hz); for input pattern *B* with 50% overlap (silhouette = 0.8286), clusters are: cluster 0 (1,859; 92.9%) low-intensity firing (mean rate: 0.40 Hz) and cluster 1 (141; 7.1%) late-task activation with high-intensity firing (10.31 Hz); for input pattern *B* with 40% overlap (silhouette = 0.8286), clusters are: cluster 0 (1,878; 93.9%) low-intensity firing (mean rate: 0.40 Hz) and cluster 1 (122; 6.1%) late-task activation with high-intensity firing (11.03 Hz).

These results indicate that the consistently high silhouette coefficients across output patterns demonstrate clear separability of GC firing patterns into 2-3 distinct clusters. Notably, low-intensity firing patterns dominate (> 90% of cells), with the remaining minority (< 10%) exhibiting moderate- to high-intensity firing. This structural consistency in output patterns persists across varying input overlap degrees, revealing similar organizational characteristics of granule cell activity. Crucially, this similarity in structural features maintains following pattern separation, evidencing conserved output pattern organization post-transformation.

4. Conclusions and discussion

This study systematically investigates how input pattern dissimilarity modulates pattern separation in DG. We developed a multi-scale DG network model spanning network, cellular, and subcellular levels to maximize biological realism. Population coding analysis of pattern pairs with systematically controlled overlaps (ranging from 80% to 40%) demonstrated that decreasing input similarity: 1) significantly increases population distance, and 2) enhances pattern orthogonality, indicating progressively improved separation efficacy. Conversely, pattern separation efficiency declined with reduced overlap.

Within a rate coding framework, we precisely characterized how input patterns modulate GC spiking dynamics: while reduced overlap preserved mean firing rates, firing rate distribution profiles, and the proportion of rate-invariant cells, the Pearson correlation coefficients and mutual information between output pattern pairs decreased significantly with diminishing overlap, further confirming enhanced pattern separation. Notably, high-overlap inputs (> 70%) induced substantial firing rate variability in individual GCs, whereas low-overlap inputs effectively minimized such fluctuations. Cluster analysis of time-windowed firing rates further revealed that reduced input overlap did not alter the structural characteristics of GC ensembles, as pattern separation maintained the similarity-based topological organization of output patterns.

This research employs multi-scale computational modeling and a dual-coding framework to systematically elucidate how input overlap regulates GC spiking dynamics and pattern separation efficacy. The established DG neural network model provides a mechanistic platform for investigating pattern separation processes. Current model limitations include the omission of rare neuronal subtypes and insufficient incorporation of dendritic computation mechanisms, which represent priority targets for subsequent investigation.

Use of AI tools declaration

The authors declare they have not used Artificial Intelligence (AI) tools in the creation of this article.

Conflict of interest

The authors declare there is no conflict of interest.

References

1. H. Eichenbaum, A cortical-hippocampal system for declarative memory, *Nat. Rev. Neurosci.*, **1** (2000), 41–50. https://doi.org/10.1038/35036213
2. B. Schmidt, D. F. Marrone, E. J. Markus, Disambiguating the similar: The dentate gyrus and pattern separation, *Behav. Brain Res.*, **226** (2012), 56–65. https://doi.org/10.1016/j.bbr.2011.08.039
3. N. Rebola, M. Carta, C. Mulle, Operation and plasticity of hippocampal CA3 circuits: implications for memory encoding, *Nat. Rev. Neurosci.*, **18** (2017), 208–220. https://doi.org/10.1038/nrn.2017.10
4. S. Y. Kim, W. Lim, Effect of adult-born immature granule cells on pattern separation in the hippocampal dentate gyrus, *Cognit. Neurodyn.*, **18** (2024), 2077–2093. https://doi.org/10.1007/s11571-023-09985-5
5. A. Treves, E. T. Rolls, Computational analysis of the role of the hippocampus in memory, *Hippocampus*, **4** (1994), 374–391. https://doi.org/10.1002/hipo.450040319
6. E. T. Rolls, R. P. Kesner, A computational theory of hippocampal function, and empirical tests of the theory, *Prog. Neurobiol.*, **79** (2006), 1–48. https://doi.org/10.1016/j.pneurobio.2006.04.005
7. R. P. Kesner, E. T. Rolls, A computational theory of hippocampal function, and tests of the theory: New developments, *Neurosci. Biobehav. Rev.*, **48** (2015), 92–147. https://doi.org/10.1016/j.neubiorev.2014.11.009
8. W. Deng, J. B. Aimone, F. H. Gage, New neurons and new memories: how does adult hippocampal neurogenesis affect learning and memory? *Nat. Rev. Neurosci.*, **11** (2010), 339–350. https://doi.org/10.1038/nrn2822
9. M. A. Yassa, C. E. L. Stark, Pattern separation in the hippocampus, *Trends Neurosci.*, **34** (2011), 515–525. https://doi.org/10.1016/j.tins.2011.06.006
10. J. J. Knierim, J. P. Neunuebel, Tracking the flow of hippocampal computation: Pattern separation, pattern completion, and attractor dynamics, *Neurobiol. Learn. Mem.*, **129** (2016), 38–49. https://doi.org/10.1016/j.nlm.2015.10.008
11. T. Hainmueller, M. Bartos, Dentate gyrus circuits for encoding, retrieval and discrimination of episodic memories, *Nat. Rev. Neurosci.*, **21** (2020), 153–168. https://doi.org/10.1038/s41583-019-0260-z

12. Y. Senzai, Function of local circuits in the hippocampal dentate gyrus-CA3 system, *Neurosci. Res.*, **140** (2019), 43–52. https://doi.org/10.1016/j.neures.2018.11.003

13. K. Nakazawa, Dentate mossy cell and pattern separation, *Neuron*, **93** (2017), 465–467. https://doi.org/10.1016/j.neuron.2017.01.021

14. D. F. Marrone, A. A. Adams, E. Satvat, Increased pattern separation in the aged fascia dentata, *Neurobiol. Aging*, **32** (2011), 2317.e23–2317.e32. https://doi.org/10.1016/j.neurobiolaging.2010.03.021

15. S. Chavlis, P. C. Petrantonakis, P. Poirazi, Dendrites of dentate gyrus granule cells contribute to pattern separation by controlling sparsity, *Hippocampus*, **27** (2017), 89–110. https://doi.org/10.1002/hipo.22675

16. P. C. Petrantonakis, P. Poirazi, Dentate gyrus circuitry features improve performance of sparse approximation algorithms, *PLoS One*, **10** (2015), e0117023. https://doi.org/10.1371/journal.pone.0117023

17. K. Yang, X. Sun, S. Zhu, The heterogeneous population of granule cells contributes to pattern separation of the dentate gyrus neural network, *Nonlinear Dyn.*, **112** (2024), 13465–13481. https://doi.org/10.1007/s11071-024-09730-5

18. D. J. Willshaw, P. Dayan, R. G. M. Morris, Memory, modelling and marr: a commentary on Marr (1971) ‘simple memory: a theory of archicortex’, *Phil. Trans. R. Soc. B*, **370** (2015), 20140383. https://doi.org/10.1098/rstb.2014.0383

19. A. D. Madar, L. A. Ewell, M. V. Jones, Pattern separation of spiketrains in hippocampal neurons, *Sci. Rep.*, **9** (2019), 5282. https://doi.org/10.1038/s41598-019-41503-8

20. F. Faghihi, A. A. Moustafa, Impaired neurogenesis of the dentate gyrus is associated with pattern separation deficits: A computational study, *J. Integr. Neurosci.*, **15** (2016), 277–293. https://doi.org/10.1142/S0219635216500175

21. S. J. Guzman, A. Schlögl, C. Espinoza, X. Zhang, B. A. Suter, P. Jonas, How connectivity rules and synaptic properties shape the efficacy of pattern separation in the entorhinal cortex–dentate gyrus–CA3 network, *Nat. Comput. Sci.*, **1** (2021), 830–842. https://doi.org/10.1038/s43588-021-00157-1

22. C. E. Myers, H. E. Scharfman, A role for hilar cells in pattern separation in the dentate gyrus: A computational approach, *Hippocampus*, **19** (2009), 321–337. https://doi.org/10.1002/hipo.20516

23. C. E. Myers, H. E. Scharfman, Pattern separation in the dentate gyrus: A role for the CA3 backprojection, *Hippocampus*, **21** (2011), 1190–1215. https://doi.org/10.1002/hipo.20828

24. C. E. Myers, K. Bermudez-Hernandez, H. E. Scharfman, The influence of ectopic migration of granule cells into the hilus on dentate gyrus-CA3 function, *PLoS One*, **8** (2013), e68208. https://doi.org/10.1371/journal.pone.0068208

25. A. Hummos, C. C. Franklin, S. S. Nair, Intrinsic mechanisms stabilize encoding and retrieval circuits differentially in a hippocampal network model, *Hippocampus*, **24** (2014), 1430–1448. https://doi.org/10.1002/hipo.22324

26. R. Coultrip, R. Granger, G. Lynch, A cortical model of winner-take-all competition via lateral inhibition, *Neural Networks*, **5** (1992), 47–54. https://doi.org/10.1016/S0893-6080(05)80006-1

27. M. J. West, L. Slomianka, H. J. G. Gundersen, Unbiased stereological estimation of the total number of neurons in the subdivisions of the rat hippocampus using the optical fractionator, *Anat. Rec.*, **231** (1991), 482–497. https://doi.org/10.1002/ar.1092310411
28. P. S. Buckmaster, A. L. Jongen-Rêlo, Highly specific neuron loss preserves lateral inhibitory circuits in the dentate gyrus of kainate-induced epileptic rats, *J. Neurosci.*, **19** (1999), 9519–9529. https://doi.org/10.1523/JNEUROSCI.19-21-09519.1999
29. D. G. Amaral, N. Ishizuka, B. Claiborne, Chapter neurons, numbers and the hippocampal network, *Prog. Brain Res.*, **83** (1990), 1–11. https://doi.org/10.1016/S0079-6123(08)61237-6
30. B. McNaughton, C. Barnes, S. Mizumori, E. Green, P. Sharp, Contribution of granule cells to spatial representations in hippocampal circuits: A puzzle, in *Kindling and Synaptic Plasticity: The Legacy of Graham Goddar*, Springer-Verlag, Boston, **110** (1991), 123.
31. T. Hafting, M. Fyhn, S. Molden, M. Moser, E. Moser, Microstructure of a spatial map in the entorhinal cortex, *Nature*, **436** (2005), 801–806. https://doi.org/10.1038/nature03721
32. R. Brette, W. Gerstner, Adaptive exponential integrate-and-fire model as an effective description of neuronal activity, *J. Neurophysiol.*, **94** (2005), 3637–3642. https://doi.org/10.1152/jn.00686.2005
33. A. Roth, M. Van Rossum, Modeling synapses, in *Computational Modeling Methods for Neuroscientists*, (2009), 139–160. https://doi.org/10.7551/mitpress/9780262013277.003.0007
34. J. Geiger, J. Lubke, A. Roth, M. Frotscher, P. Jonas, Submillisecond AMPA receptor-mediated signaling at a principal neuron-interneuron synapse, *Neuron*, **18** (1997), 1009–1023. https://doi.org/10.1016/S0896-6273(00)80339-6
35. C. Schmidt-Hieber, J. Bischofberger, Fast sodium channel gating supports localized and efficient axonal action potential initiation, *J. Neurosci.*, **30** (2010), 10233–10242. https://doi.org/10.1523/JNEUROSCI.6335-09.2010
36. R. Krueppel, S. Remy, H. Beck, Dendritic integration in hippocampal dentate granule cells, *Neuron*, **71** (2011), 512–528. https://doi.org/10.1016/j.neuron.2011.05.043
37. P. H. Chiang, P. Y. Wu, T. W. Kuo, Y. C. Liu, C. F. Chan, T. C. Chien, et al., Gaba is depolarizing in hippocampal dentate granule cells of the adolescent and adult rats, *J. Neurosci.*, **32** (2012), 62–67. https://doi.org/10.1523/JNEUROSCI.3393-11.2012
38. P. J. Rousseeuw, Silhouettes: A graphical aid to the interpretation and validation of cluster analysis, *J. Comput. Appl. Math.*, **20** (1987), 53–65. https://doi.org/10.1016/0377-0427(87)90125-7

AIMS Press